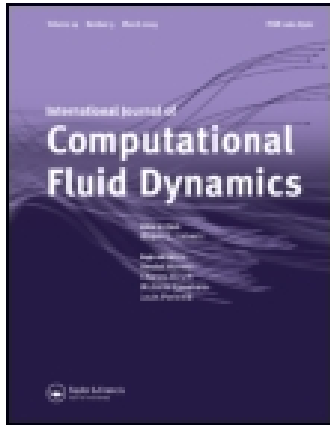


This article was downloaded by: [Imperial College London Library]

On: 15 December 2014, At: 01:45

Publisher: Taylor & Francis

Informa Ltd Registered in England and Wales Registered Number: 1072954 Registered office: Mortimer House, 37-41 Mortimer Street, London W1T 3JH, UK



## International Journal of Computational Fluid Dynamics

Publication details, including instructions for authors and subscription information:

<http://www.tandfonline.com/loi/gcfd20>

### A DNS study of jet control with microjets using an immersed boundary method

Rémi Gautier<sup>a</sup>, Sylvain Laizet<sup>b</sup> & Eric Lamballais<sup>a</sup>

<sup>a</sup> Department of Fluid Flow, Heat Transfer and Combustion, Institute PPRIME, Université de Poitiers, CNRS, ENSMA, Futuroscope Chasseneuil Cedex, France

<sup>b</sup> Turbulence, Mixing and Flow Control Group, Department of Aeronautics, Imperial College London, London, UK

Published online: 08 Sep 2014.



CrossMark

[Click for updates](#)

To cite this article: Rémi Gautier, Sylvain Laizet & Eric Lamballais (2014) A DNS study of jet control with microjets using an immersed boundary method, International Journal of Computational Fluid Dynamics, 28:6-10, 393-410, DOI: [10.1080/10618562.2014.950046](https://doi.org/10.1080/10618562.2014.950046)

To link to this article: <http://dx.doi.org/10.1080/10618562.2014.950046>

PLEASE SCROLL DOWN FOR ARTICLE

Taylor & Francis makes every effort to ensure the accuracy of all the information (the "Content") contained in the publications on our platform. However, Taylor & Francis, our agents, and our licensors make no representations or warranties whatsoever as to the accuracy, completeness, or suitability for any purpose of the Content. Any opinions and views expressed in this publication are the opinions and views of the authors, and are not the views of or endorsed by Taylor & Francis. The accuracy of the Content should not be relied upon and should be independently verified with primary sources of information. Taylor and Francis shall not be liable for any losses, actions, claims, proceedings, demands, costs, expenses, damages, and other liabilities whatsoever or howsoever caused arising directly or indirectly in connection with, in relation to or arising out of the use of the Content.

This article may be used for research, teaching, and private study purposes. Any substantial or systematic reproduction, redistribution, reselling, loan, sub-licensing, systematic supply, or distribution in any form to anyone is expressly forbidden. Terms & Conditions of access and use can be found at <http://www.tandfonline.com/page/terms-and-conditions>

## A DNS study of jet control with microjets using an immersed boundary method

Rémi Gautier<sup>a</sup>, Sylvain Laizet<sup>b</sup> and Eric Lamballais<sup>a,\*</sup>

<sup>a</sup>Department of Fluid Flow, Heat Transfer and Combustion, Institute PPRIME, Université de Poitiers, CNRS, ENSMA, Futuroscope Chasseneuil Cedex, France; <sup>b</sup>Turbulence, Mixing and Flow Control Group, Department of Aeronautics, Imperial College London, London, UK

(Received 17 March 2014; accepted 21 July 2014)

In this work, a microjet arrangement to control a turbulent jet is studied by means of direct numerical simulation. A customised numerical strategy was developed to investigate the interactions between the microjets and the turbulent jet. This approach is based on an improved immersed boundary method in order to reproduce realistically the control device while being compatible with the accuracy and the parallel strategy of the in-house code `Incompact3d`. The 16 converging microjets, so-called *fluidevrons*, lead to an increase of the turbulent kinetic energy in the near-nozzle region through an excitation at small scale caused by the interaction between the *fluidevrons* and the main jet. As a consequence, very intense unstable ejections are produced from the centre of the jet toward its surrounding. Further downstream, the turbulent kinetic energy levels are lower with a lengthening of the potential core compared to a natural jet, in agreement with experimental results.

**Keywords:** direct numerical simulation; immersed boundary method; turbulent jet; microjet control

### 1. Introduction

A large number of studies in the literature have focused on the control of a jet, mainly with two objectives: the control of the mixing properties of the jet (Raman 1997; Lardeau, Lamballais, and Bonnet 2002) and for noise reduction purposes (Arakeri et al. 2003; Castelain et al. 2008; Laurendeau et al. 2008; Maury et al. 2012). The objective of the present numerical work is to help in our understanding of aeroacoustic mechanisms in the context of fluidic control. More precisely, the idea is to propose control solutions of the acoustic sources of a jet. A microjet device is used in order to modify the near-nozzle region of the main jet. Various effects can be obtained by playing with the number of microjets and their arrangement. Here, we focus on a configuration with 16 microjets organised as 8 pairs of 2 converging microjets where each pair of converging microjets produces a chevron-like excitation. An illustration of the experimental device, used by Maury et al. (2012), can be seen in Figure 1 (left). The main advantage of such a device by comparison to a nozzle with classic chevrons is its flexibility, with the ability to activate/deactivate easily the control. For aeronautic applications, it means that it is possible to suspend the control during flight mode (when the jet engine can keep its optimal performance) and only activate the *fluidevrons* control during landing and take-off when a noise reduction is needed.

The present numerical work is a complement of previous experimental studies with the same type of set-up (Laurendeau et al. 2008; Maury et al. 2009). In this paper, on top of presenting the numerical challenge for the modelling of the experimental device in the computational domain, discussions focus on the characteristics of the flow in a context of an incompressible regime. The idea is to better understand the effects of the microjet device observed experimentally, with a particular emphasis on how the perturbations in the near-nozzle region impact the streamwise evolution of the main jet.

From a numerical point of view, there are many obstacles that need to be overtaken for a realistic reproduction of the experimental set-up by means of direct numerical simulation (DNS). First, the Reynolds number of the flow must be high enough in order to allow comparisons with the experiments. This requires the use of a very fine mesh in space combined with a very accurate strategy for the resolution of the incompressible Navier–Stokes equations. The in-house finite difference code `Incompact3d` is the right tool to address such simulations as it is based on high-order schemes (Laizet and Lamballais 2009) and can be combined with a powerful two-dimensional (2D) domain decomposition library (Li and Laizet 2010) for use on supercomputers.

Then, the main technical problem is the realistic modelling of the microjet device. One possibility is to use a

\*Corresponding author. Email: [eric.lamballais@univ-poitiers.fr](mailto:eric.lamballais@univ-poitiers.fr)

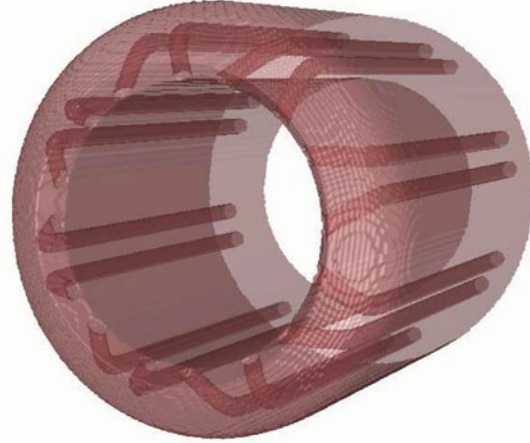
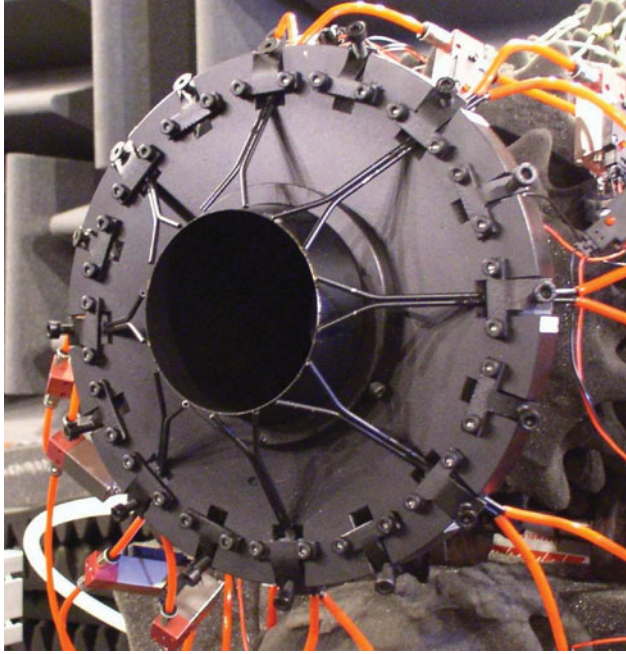


Figure 1. Experimental device (left) from Maury et al. (2009) and numerical device (right) reproduced through an immersed boundary method (IBM).

localised forcing to take into account the effect of the fludevrons (Shur, Spalart, and Strelets 2010). However, this approach is not realistic enough for a detailed analysis of the interaction between the microjets and the main jet. The strategy proposed in the present work is to explicitly reproduce the interaction by modelling the geometry of the nozzle with the microchannels as shown in Figure 1 (right). To achieve this, an improved immersed boundary method (IBM) is used. The main advantage of this approach is that it is possible to reproduce a complex geometry on a simplified mesh (the code `Incompact3d` is based on a Cartesian mesh). Unfortunately, keeping a good accuracy is not easy in the near-obstacle region, in particular when high-order schemes are used for the spatial differentiation. Furthermore, the IBM must be compatible with the 2D domain decomposition library that is used in `Incompact3d` in order to keep the performance of the code on supercomputers.

The paper is organised as follow: after a description of the flow configuration and the numerical methods in Section 2, the improved IBM is described in Section 3. Then, Sections 4 and 5 are dedicated to the validation of the improved IBM for an academic case and for a natural jet where the nozzle is taken into account inside the computational domain. The results obtained with the microjet device are presented in Section 6, with some comparisons with the natural jet. The paper is ended with a conclusive section with discussions about the perspectives for the improved IBM and about the physical analysis that remains to be done for

an optimum control of a turbulent jet with fludevrons for aeroacoustic applications.

## 2. Problem description and modelling approach

### 2.1. Flow configuration

We consider a main jet at the exit of a nozzle of internal diameter  $D$ . Part of the nozzle is included inside the computational domain  $L_x \times L_y \times L_z$  as shown in Figure 1 (right). The Reynolds number is  $\text{Re} = U_c D / \nu = 10,000$  where  $U_c$  is the velocity of the jet on the centreline at the exit of the nozzle. The coordinate system  $\mathcal{R}$  is orthonormal with coordinate  $x$  in the streamwise direction and coordinates  $(y, z)$  in the transverse plane such that  $y = z = 0$  on the centreline. The origin of  $\mathcal{R}$  is shown in Figure 2 and is located just at the exit of the nozzle on the centreline of the main jet, at a distance  $2D$  from the upstream side of the computational domain. For the inflow boundary condition at  $x = -2D$ , the velocity profile inside the nozzle is based on a mean profile  $U(r) = [1 - (2r/D)^6]U_c$  with  $r = \sqrt{y^2 + z^2}$  (corresponding to the radial coordinate). The synthetic turbulent perturbations superimposed on this mean profile are expressed as follows:

$$u'_i(r, \theta, t) = \mathcal{A}(r) \sum_{n=1}^m a'_n(t) \cos(n\theta + \Phi'_n(t)) \quad (1)$$

where  $m$  is the number of excited modes in the azimuthal direction of coordinate  $\theta$ ,  $t$  the time and  $(a_n, \Phi_n)$  the amplitude

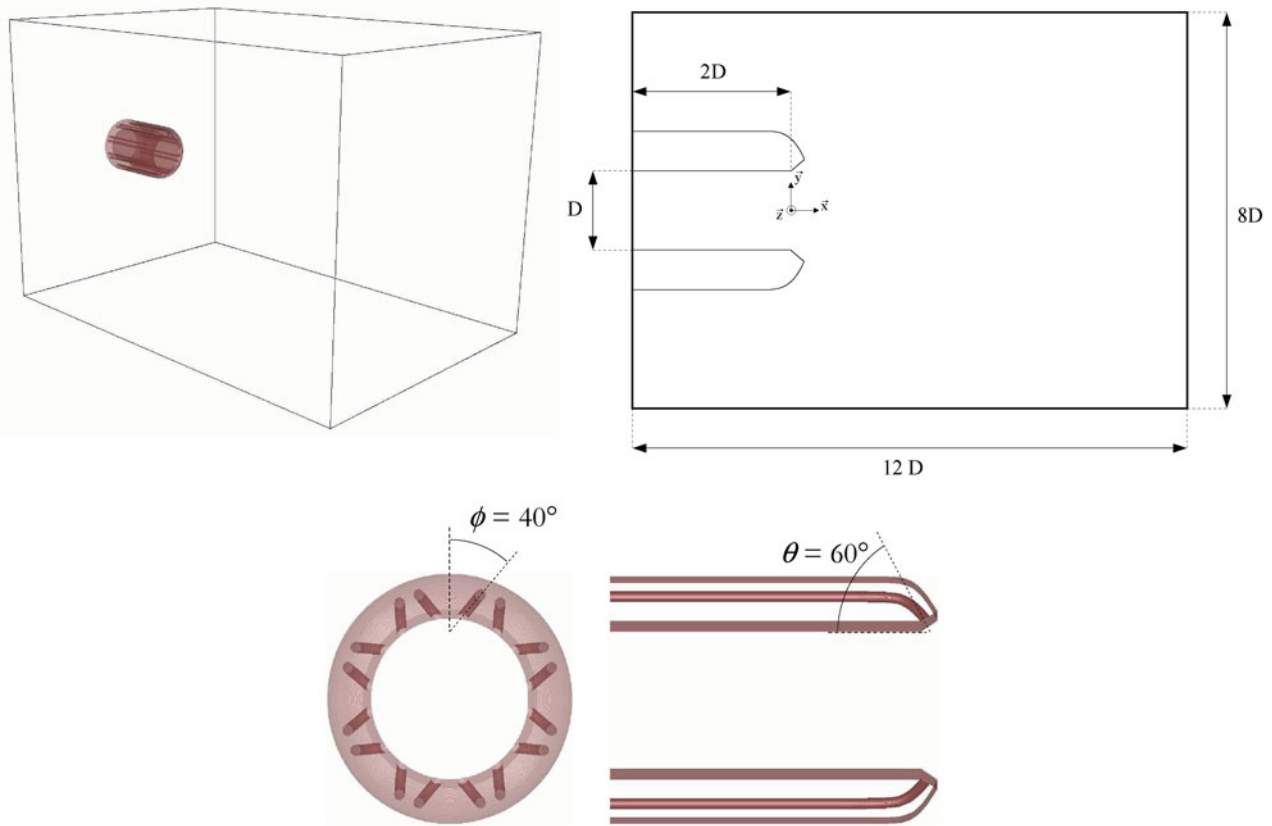


Figure 2. Top left: perspective view of the computational domain with the jet nozzle. Top right: side view with the main geometric parameters (not to scale). Bottom: angles of convergence ( $\phi = 40^\circ$ ) and penetration ( $\theta = 60^\circ$ ).

and phase generated randomly up to a cut-off frequency. This spatially and temporally correlated noise avoids the excitation of spurious spatial and time scales that cannot be described by the computational mesh. The modulation function  $\mathcal{A}(r)$  is used in order to satisfy the no-slip boundary condition for  $r = D/2$  while keeping the perturbations maximal for  $r = 0.484D$ . The shape of the mean profile and the modulation and amplitude of the perturbations have been carefully chosen to match the experimental data at the exit of the nozzle. This point will be examined in Section 5 for validation.

For the controlled case, each microjet is generated inside a microchannel of diameter  $d$  located inside the nozzle with  $D/d = 15$ . The exit of the microchannel is located just at the lip of the nozzle. At the upstream side of the computational domain, a Poiseuille profile is imposed in each microchannel. The orientation of the microchannels is defined with the penetration angle  $\theta = 60^\circ$  and the convergence angle  $\phi = 40^\circ$  as shown in Figure 2. Note that the velocity around the nozzle is not zero with the imposition of a small co-flow of velocity equal to  $4\%U_c$ . This co-flow avoids dealing with stagnant flow near the outlet, a situation that is very critical for any outflow boundary conditions in

incompressible flows. In order to ensure the no-slip boundary condition for the outside wall of the nozzle, a laminar boundary profile is imposed with a thickness of about nine meshes.

At the outlet of the computational domain for  $x = L_x$ , a simplified convection equation is imposed whereas for the lateral sides ( $y = \pm L_y/2$  and  $z = \pm L_z/2$ ), modified Dirichlet boundary conditions are imposed, following a procedure described in Hasan, Anwer, and Sanghi (2005). The idea is to allow the flow to enter the domain in order to mimic an entrainment mechanism. Note that for the computational domain used in the present study, the aspiration of fluid was marginal, with no significant impact by comparison to more classic free-slip boundary conditions.

## 2.2. Numerical methods

The in-house code `Incompact3d1` is used to solve the incompressible Navier–Stokes equations

$$\frac{\partial u_i}{\partial t} + \frac{1}{2} \left( u_j \frac{\partial u_i}{\partial x_j} + \frac{\partial u_i u_j}{\partial x_j} \right) = -\frac{1}{\rho} \frac{\partial p}{\partial x_i} + \nu \frac{\partial^2 u_i}{\partial x_j \partial x_j} \quad (2)$$

$$\frac{\partial u_i}{\partial x_i} = 0 \quad (3)$$

where  $p(x_j, t)$  is the pressure field (for a fluid with a constant density  $\rho$ ),  $u_i(x_j, t)$  the velocity field and  $\nu$  the kinematic viscosity. Note that convective terms are written in the skew-symmetric form. This specific form is used in this study as it allows the reduction of aliasing errors while remaining energy conserving for the spatial discretisation permitted in the code (Kravchenko and Moin 1997). The computational domain  $L_x \times L_y \times L_z = 12D \times 8D \times 8D$  is discretised on a Cartesian mesh of  $n_x \times n_y \times n_z = 1025 \times 1025 \times 1025$  mesh points, split into 2048 computational cores. This resolution has been carefully chosen to allow the correct reproduction of the finest scales of the flow, and in particular of the flow inside the microchannels.

The spatial discretisation is achieved with sixth-order compact schemes (Lele 1992) while the time advancement is performed with a classic second-order Adams–Bashforth scheme. The main originality of the code `Incompact3d` is that the Poisson equation to insure incompressibility is fully solved in spectral space via the use of relevant three-dimensional (3D) fast Fourier transforms (FFT). With the help of the concept of modified wavenumber, the divergence-free condition is ensured up to machine accuracy. The pressure mesh is staggered from the velocity one by half a mesh to avoid spurious pressure oscillations observed in a fully collocated approach (Laizet and Lamballais 2009). To control the aliasing errors, an artificial dissipation is applied through the viscous terms following a strategy proposed by Lamballais, Fortuné, and Laizet (2011). Note that this numerical dissipation is only active at the scales with a wavelength close to two spatial meshes. Finally, because of the size of the simulations, the parallel version of the code has been used for this numerical work. More details about the efficient parallel strategy, based on a highly scalable 2D decomposition library and a distributed FFT interface, can be found in Laizet and Li (2011).

For the present study, an IBM is needed in order to take into account the nozzle with the microjet device inside the computational domain based on a Cartesian mesh. In the context of direct and large eddy simulations (DNS/LES), the code `Incompact3d` has already been combined with an IBM based on a feedback forcing (Goldstein, Handler, and Sirovich 1993) for various configurations of the flow around a cylinder (Silvestrini and Lamballais 2002; Lamballais and Silvestrini 2002; Silvestrini and Lamballais 2004). More recently, an approach based on a direct forcing (Fadlun et al. 2000), suitable for high-order schemes (Parnaudeau et al. 2008), has been successfully used for various flow configurations (see for instance Lamballais, Silvestrini, and Laizet 2008, 2010; Lamballais 2014). In the present case, the geometry of the nozzle with the microjet device is extremely complex and the previous IBMs are not

suitable to impose the no-slip boundary conditions where needed while being compatible with the use of high-order schemes for the spatial discretisation. The details about the new improved IBM are presented in Section 3.

In a general framework, the temporal advancement for one time step  $\Delta t = t_{n+1} - t_n$  for the convective and diffusive terms is done explicitly using a second-order Adams–Bashforth scheme. Combined with a fractional step method for the incompressibility (Chorin 1968; Temam 1969), the time advancement can be written as

$$\frac{u_i^* - u_i^n}{\Delta t} = \frac{3}{2} F_i^n - \frac{1}{2} F_i^{n-1} - \frac{1}{\rho} \frac{\partial p^{n-\frac{1}{2}}}{\partial x_i} \quad (4)$$

$$\frac{u_i^{**} - u_i^*}{\Delta t} = \frac{1}{\rho} \frac{\partial p^{n-\frac{1}{2}}}{\partial x_i} \quad (5)$$

$$\frac{u_i^{n+1} - u_i^{**}}{\Delta t} = -\frac{1}{\rho} \frac{\partial p^{n+\frac{1}{2}}}{\partial x_i} \quad (6)$$

with

$$F_i^n = -\frac{1}{2} \left( u_j^n \frac{\partial u_i^n}{\partial x_j} + \frac{\partial u_i^n u_j^n}{\partial x_j} \right) + \nu \frac{\partial^2 u_i^n}{\partial x_j \partial x_j} \quad (7)$$

and  $u_i^n = u_i(x_j, t_n)$ . At this stage, the IBM does not explicitly appear in these equations. However, it is important to notice that the evaluation of  $u_i^*$ ,  $u_i^{**}$  and  $u_i^{n+1}$  in Equations (4)–(6) does only make sense in the fluid region.

In order to distinguish fluid and solid regions in the computational domain, a field  $\varepsilon(x_i)$  can be defined, which is equal to 1 in the solid regions and equal to 0 in the fluid regions. Using  $\varepsilon$ , it is possible to impose a no-slip boundary condition (at least for non-moving solid regions) via a direct forcing imposing  $u_i^* = 0$  when  $\varepsilon = 1$  in Equation (4), in order to verify  $u_i^{n+1} \approx 0$ . Imposing the forcing on  $u_i^*$  instead of  $u_i^{n+1}$  allows us to be more flexible with the incompressibility condition on  $u_i^{n+1}$  while being more robust from a numerical point of view.

Following the idea of Parnaudeau et al. (2008), a modified Poisson equation is solved in the solid regions which can be expressed as

$$\frac{1}{\rho} \frac{\partial^2 p^{n+\frac{1}{2}}}{\partial x_i \partial x_i} = \frac{1}{\Delta t} \frac{\partial \left( (1 - \varepsilon^-) \bar{u}_i^* \right)}{\partial x_i} \quad (8)$$

where  $\varepsilon^-$  corresponds to  $\varepsilon$  with a one-mesh retraction from the solid regions. For the present flow configuration, preliminary tests showed that it is preferable to use  $\varepsilon^-$  instead of  $\varepsilon$  in Equation (8) as it allows a better mass conservation near the solid regions. Despite the marginal spatial resolution of the microchannels for the present configuration with about eight mesh points in the radial directions to describe one microchannel diameter  $d$ , it is extremely important to satisfy the mass conservation in order to obtain the expected flow

rate at the exit of the nozzle.<sup>2</sup> When  $\varepsilon^- = 0$ , the classic Poisson equation is recovered, satisfying the incompressibility condition on  $u_i^{n+1}$ . When  $\varepsilon^- = 1$ ,  $p^{n+\frac{1}{2}}$  satisfies a Laplace equation with no physical meaning nevertheless being consistent with the pressure in the fluid region.

It should be noted that the forcing term associated with the IBM does not appear in Equation (4) because this equation does not need to be solved where  $\varepsilon = 1$ . Furthermore, the condition  $u_i^* = 0$  in Equation (4) and in the correction steps (5) and (6) only makes sense at the interface regions for which  $\varepsilon - \varepsilon^- = 1$ . The new strategy proposed here is based on the indirect imposition of  $u_i^* = 0$  at the immersed boundary during the computation of the spatial derivatives in  $F_i^n$  with no explicit forcing when  $\varepsilon = 1$ . The idea behind this approach is that it is possible to artificially extend the solution from fluid regions into solid regions while keeping the no-slip boundary condition at the wall and the regularity of the solution for the entire computational domain. The implementation of this improved IBM is detailed in the next section.

### 3. Alternating direction forcing strategy

The simplest method of direct forcing is to use Equations (4)–(6) in fluid regions where  $\varepsilon = 0$  while imposing  $u_i^* = 0$  in Equation (4) in solid regions where  $\varepsilon = 1$ . It leads to  $u_i^{n+1} \approx 0$  after the correction steps (5) and (6) and can be used for the evaluation of  $F_i^n$  at the next time step. Indeed, to compute  $F_i^n$ , it is necessary to know  $u_i^n$  for the entire computational domain in order to evaluate the velocity field while keeping the homogeneity of the spatial operators for  $\varepsilon = 1$  and  $\varepsilon = 0$  and also at the interface between solid and fluid regions. The homogeneity for the spatial operators is crucial for the robustness of an IBM and is a serious advantage by comparison to a strategy based on a body fitted approach. However, the condition  $u_i^{n+1} \approx 0$  everywhere in solid regions does not allow a smooth solution at the interface between solid and fluid regions because the continuity of the spatial derivatives cannot be ensured.

When combined with low-order schemes, this loss of continuity has only a minor impact on the solution. However, when combined with high-order schemes, it can generate spurious oscillations on the derivatives at the interface between solid and fluid regions. It is even worse when Hermitian compact schemes are used, such as the ones in *Incompact3d*. In order to deal with this problem, Parnaudeau et al. (2008) decided to impose a non-zero velocity field inside solid regions, especially targeted to keep the no-slip boundary condition at the wall and to remove the discontinuities on the spatial derivatives. This strategy was very useful for basic geometries like a cylinder. However, it is clear that the imposition of such a targeted velocity field in solid regions is almost impossible to achieve when

the geometry is too complex. Indeed, for this approach, it is necessary to evaluate the exact location of the geometry (that does not necessarily fit the Cartesian mesh) while considering the orientation of the solid wall. For complex body, these requirements can lead to conflicts for the generation of the target velocity due to multiple cut-cell or normal direction situations. The resulting algorithm complexity is also against the computational efficiency, especially in the context of massively parallel computing.

In the present study, an improved IBM is proposed. The new method is based on a one-dimensional (1D) expansion of the solution from fluid regions into solid regions. From a practical point of view, this expansion is performed in the direction where a spatial derivative is evaluated. As a consequence, a different expansion has to be generated depending on the spatial direction of the computed derivatives. The expansion is calibrated in order to ensure the no-slip boundary condition at the wall while keeping smooth the solution to avoid any discontinuity at the interface between solid and fluid regions. This 1D approach consists in associating in each spatial direction a specific forcing. This is why the forcing associated with this method is referred as an ‘alternating direction forcing’.

Numerically, the smoothing is based on 1D expansions of the solution inside solid regions. For this work, we decided to use Lagrangian polynomial, but other options are of course available since the approach is essentially 1D. In addition, for a solid geometry fully immersed inside the computational domain, a polynomial reconstruction allows an automatic reconnection of the solution within the geometry. The resulting method is highly flexible by allowing any kind of geometries with no need to estimate the distance and normal direction with respect to the closest wall.

The polynomial reconstruction approach is illustrated in Figure 3 for a fully immersed situation (i.e. including reconnection). The filled red points represent the reconstructed solution inside the solid region from information collected in the fluid region. In the present work, the Lagrangian polynomial used for the expansion matches exactly the solution from the reference mesh points inside the fluid region. In the example from Figure 3, three reference mesh points are used (filled blue points) on each side of the solid region. Because the reconstruction of the solution concerns the velocity field, the Lagrangian polynomial is defined to satisfy the no-slip boundary condition at the solid/fluid interface, which means that in the present work, the Lagrangian polynomial order is 8. It should be noted that for stability reasons, the first mesh points outside the solid region are not included in the reference mesh points for the polynomial reconstruction (empty blue points). In fact, for a given geometry, the first mesh points after the solid/fluid interface can be extremely close to the interface. In preliminary tests, it was noticed that this situation can lead to numerical instabilities due to a too singular polynomial reconstruction.

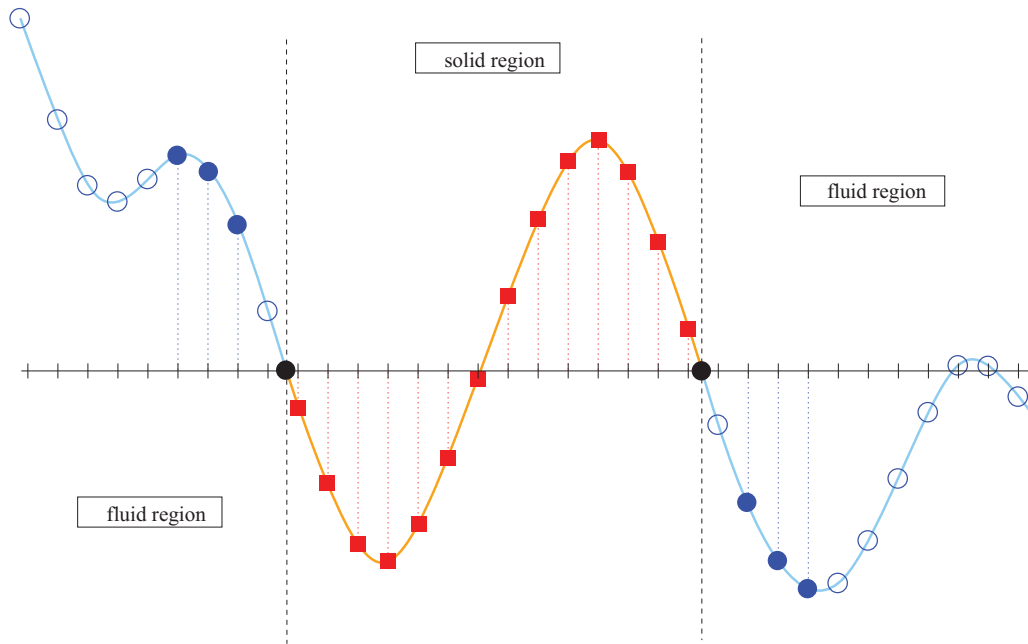


Figure 3. Schematic view of the polynomial reconstruction based on a Lagrangian polynomial. The solid/fluid interface can be identified with the black points.

It is important to point out that such a polynomial reconstruction has two drawbacks, therefore reducing its potential. First, the solid regions must be thick enough to allow a reconstruction using a minimum number of mesh points. Therefore, the modelling of an infinitely thin plate is for instance not possible. Second, it is necessary to have fluid regions wide enough, extended on at least three mesh points for the polynomial reconstruction illustrated in Figure 3. For a narrower fluid region, it is possible to use a lower order for the Lagrangian polynomial but this could slightly damage the quality of the reconstruction if the order is too low. For the present geometry of a jet nozzle with microchannels, this situation can occur near the microchannels, but with not significant damage on the quality of the solution.

The last point of this section concerns the representation of the geometry on a Cartesian mesh. If it is simple enough to be expressed analytically, the exact location of the solid/fluid interface can be known (black points in Figure 3). For more complex situations, the geometry needs to be approximated. In the present work, the geometry has been iteratively generated by joining different pre-defined parts together while performing an extrusion to shape the microchannels. This iterative procedure was fully performed on a fine mesh, 10 times smaller than the one used for the simulation in each direction. This spatial resolution of the interface location was considered to be accurate enough to avoid any stair effect in the representation of the geometry.

#### 4. Validation with the flow around a cylinder for $Re = 40$

In order to validate the new IBM, we consider in this section the steady flow around a cylinder, created by a constant velocity  $U$  over a circular cylinder of diameter  $D$  at  $Re = UD/\nu = 40$ . This not so trivial flow, with separation and recirculation regions, has been extensively studied and is well documented for the validation of IBM. Very recently, a reference solution for this flow was proposed by Gautier, Biau, and Lamballais (2013). It is accessible for any position around the cylinder thanks to a spectral interpolation subroutine. This solution can be considered as almost ‘exact’ because of its spectral accuracy and can be used for a convergence study where the errors are larger than  $10^{-11}$  for the velocity.

Validation simulations are performed on a computational domain  $L_x \times L_y = 20D \times 12D$  with a resolution of  $n_x \times n_y = 361 \times 217$  mesh points. Two other resolutions are also performed by increasing the number of mesh nodes successively by a factor 2 in both spatial directions. At the boundary of the computational domain, Dirichlet boundary conditions are imposed for the velocity with the values extracted from the reference solution. In this framework, two IBMs to model the cylinder are compared in this section.

The first one is the simplest one. The velocity field is forced to 0 ( $u_i^* = 0 \rightarrow u_i^{n+1} \approx 0$ ) in the cylinder when  $\varepsilon = 1$ . As already stated in the previous section, the main drawback of this approach is the discontinuities for the spatial derivatives at the solid/fluid interface. As a

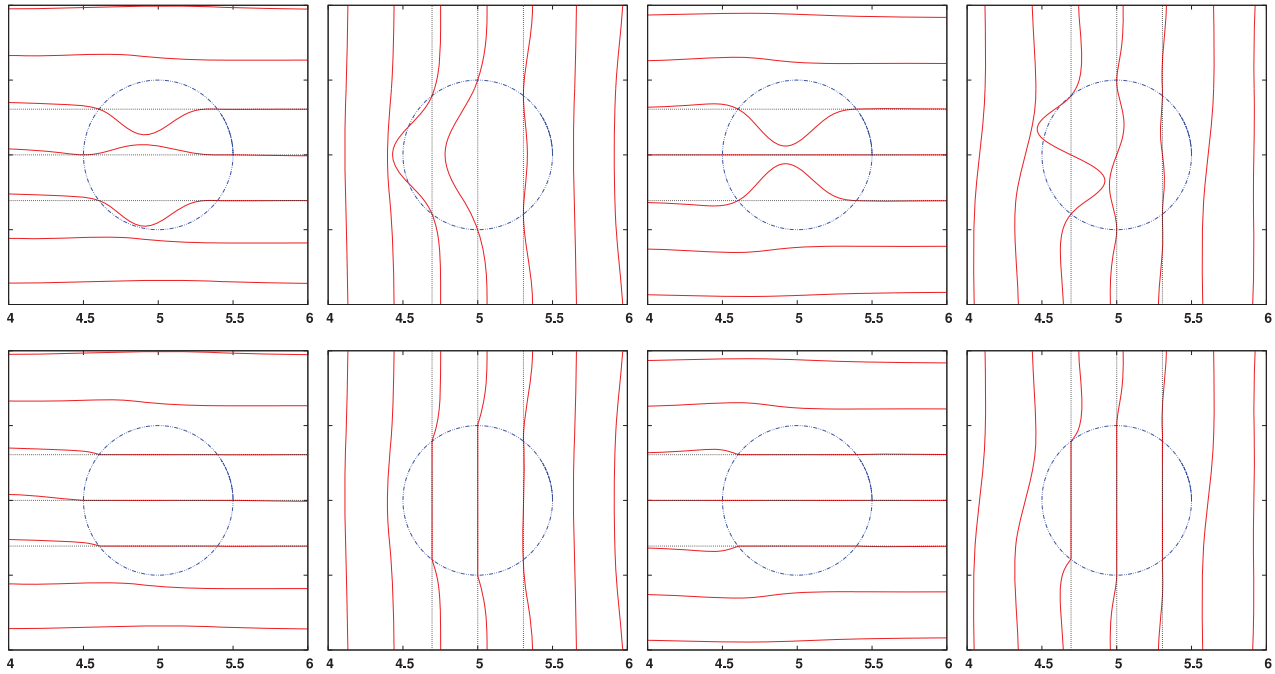


Figure 4. From left to right: profiles of  $u(x, y_c)$ ,  $u(x_c, y)$ ,  $v(x, y_c)$ ,  $v(x_c, y)$  where  $(u, v)$  are the velocity components in the streamwise and lateral directions  $(x, y)$ .  $(x_c, y_c)$  are fixed positions regularly spaced by  $\Delta_c = 0.306 D$  from the cylinder centre. Top: alternating direction forcing. Bottom: standard forcing through  $u_i^* = 0$  in the cylinder.

consequence, spurious oscillations are contaminating the solution. Furthermore, such a brutal approach does not take into account the exact location of the cylinder and the cylinder looks like a combination of stair patterns, following the Cartesian mesh. Interpolation could be performed to improve the representation of the cylinder (Fadlun et al. 2000), but the discontinuities for the spatial derivatives would still be there. This problem is shown in Figure 4 where the lack of regularity for the velocity field can be observed when the solution crosses the cylinder. Combined with a differentiation based on high-order schemes, this IBM leads to spurious oscillations.

The second method is based on the polynomial reconstruction described in the previous section. For this approach, the velocity field in the cylinder is not defined but the mesh points inside the cylinder are used for the reconstruction/reconnection based on the solution inside the fluid region (while of course ensuring the no-slip boundary condition at the wall of the cylinder). An illustration of this method is shown in Figure 4 where the velocity profiles are plotted. Note that the presented velocity data are as they are computed in the fluid region and as they are reconstructed in the solid region. Because of the 1D nature of the improved IBM, each of the two velocity components is reconstructed twice, one time per direction, leading to four reconstructions. The regularity of the solution can clearly be seen at the solid/fluid interface. For the use of high-order schemes blind with respect to the solid/fluid interface, it is

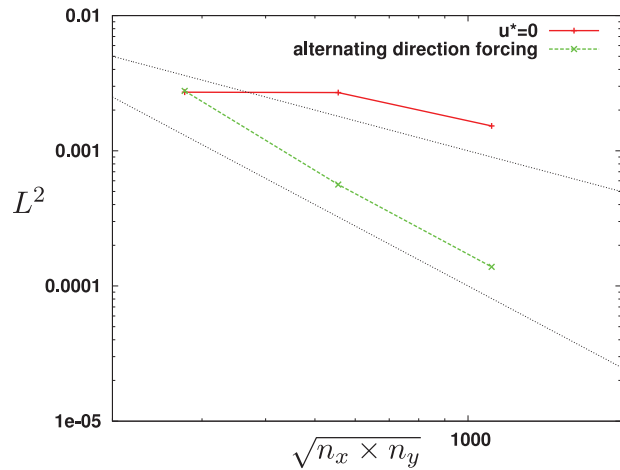


Figure 5. Error decrease of the  $L^2$  norm of the velocity as a function of  $\sqrt{n_x \times n_y}$ .

easy to understand the benefit of this approach. The resulting smoothness of the solution everywhere in the computational domain avoids the generation of spurious oscillations in derivative calculation. The reduction of oscillations near the immersed boundary was confirmed by inspecting the vorticity field (not presented here).

In practice, the main advantage of the reconstruction is not only qualitative but also quantitative. To have an estimate of this second feature, Figure 5 shows the convergence

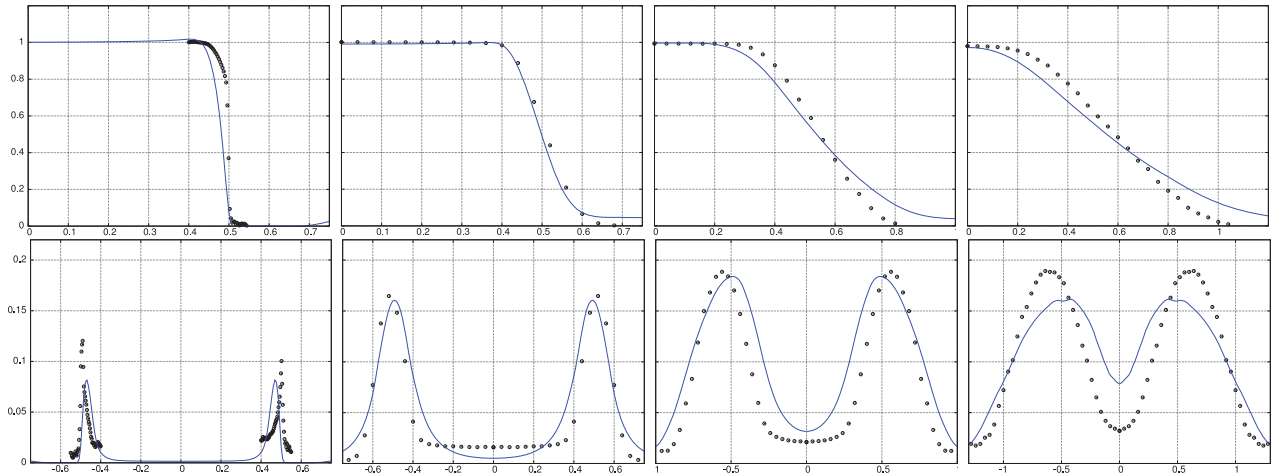


Figure 6. Profiles for the mean streamwise velocity  $\langle u \rangle(x_c, y)$  (top) and for its associated fluctuating component  $\sqrt{\langle u'u' \rangle}(x_c, y)$  (bottom) for  $x_c/D = 0.025, 1, 2.5, 4.5$  (from left to right). Comparison between our DNS (lines) and the experimental data of Maury et al. (2012) (symbols).

of the solution (expressed as the  $L^2$  norm) toward the reference solution from Gautier, Biau, and Lamballais (2013) for the two methods presented in this section. We can observe a second-order convergence for our new alternating direction forcing strategy whereas the convergence for the brutal forcing with  $u_i^* = 0$  is of order less than 1. For the highest resolution, it can be observed that the alternating direction forcing can provide an error reduction of one order of magnitude, which is a considerable improvement of the IBM accuracy.

One could expect to obtain a convergence of an order larger than 2 considering that the code `Incompact3d` is based on sixth-order schemes. However, the fact is that there is no particular treatment for the pressure field at the solid/fluid interface. This feature limits the level of the convergence to an order 2 for the velocity field and to an order 1 for the pressure field (Gautier, Biau, and Lamballais 2013). Note that this limitation in terms of asymptotic behaviour does not degrade the effects of the use of high-order schemes for 3D instationary problems. Indeed, even if the formal order of the solution is quite low near the solid/fluid interface, the quality of the reproduction of the small-scale motions is still very sensitive to the accuracy of the schemes used for the spatial differentiations. This sensitivity was shown in Parnaudeau et al. (2004) and was also taken into account for the generation of the LES database of the flow around a cylinder at  $Re = 3900$  provided by Parnaudeau et al. (2008).

## 5. Validation with a natural jet

As discussed in Section 2.1, the shape of the mean profile, the modulation and amplitude of the perturbations have been carefully chosen to match the experimental data of Maury et al. (2012) for a natural jet with no control. In the

experiment, the short length of the nozzle after the convergent (see Figure 1) leads to a non-developed pipe flow at the nozzle exit. The experimental data at the corresponding location (here, for  $x = 0.025D$ ) exhibit a top hat shape for the mean streamwise velocity profile with turbulent fluctuations concentrated in the shear region of the profile (see Figure 6). A good agreement can be seen at  $x = 0.025D$  between the experimental and numerical data, validating the numerical set-up. A more accurate agreement would not make sense as the experimental conditions are not the same as the numerical ones, in particular in terms of Reynolds number that is reduced by a factor 70 in the present numerical work, from 700,000 in the experiment to 10,000 in the DNS. The other significant difference is the co-flow for the simulation, equal to  $4\%U_c$ .

Despite these differences, a reasonably good agreement is obtained between the experiment and the simulation for the streamwise evolution of the mean streamwise velocity and its associated fluctuating component. The decrease of the mean streamwise velocity leads to a length for the potential core equal to  $5.5D$ . It is estimated to be between  $5.5D$  and  $6D$  in the experiment. The agreement between experiment and simulation can be investigated more in details in Figure 6 where the data are presented for  $x/D = 0.025, 1, 2.5, 4.5$ . For  $x = D$  and  $x = 2.5D$ , the agreement is satisfactory despite the Reynolds number difference. Further downstream, for instance for  $x = 4.5D$ , there is a significant discrepancy for the mean streamwise velocity profiles as shown in Figure 6 and Figure 7. For the same location, the profiles for  $u'_{\text{rms}}$  confirm this trend with a substantial deviation between the numerical and experimental profiles. It appears that the maxima for  $u'_{\text{rms}}$  diminish whereas they slightly increase in the experiment. Conversely, on the centreline of the jet, the perturbations are over-estimated in the simulation. This can be linked to the lower Reynolds

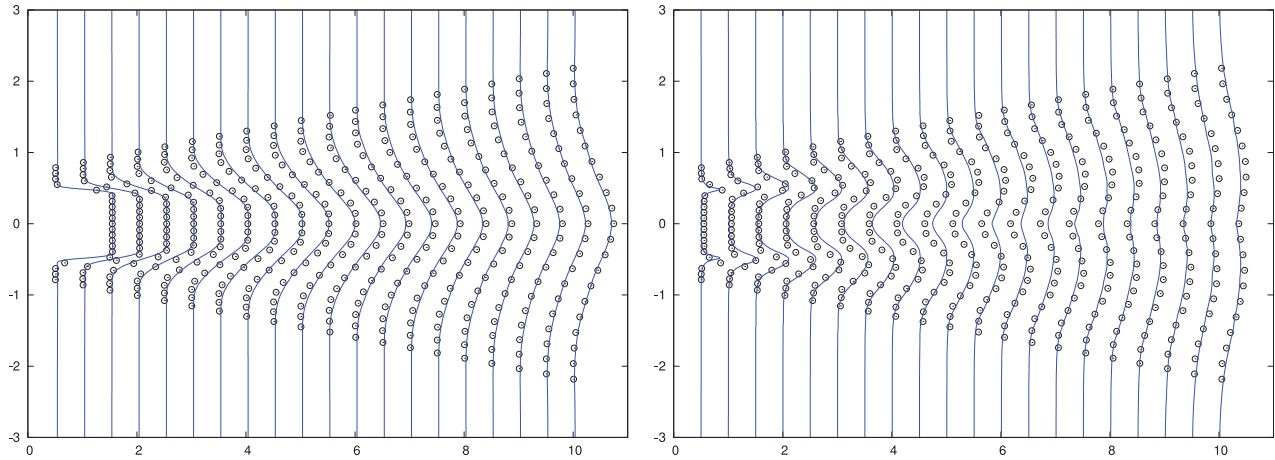


Figure 7. Profiles for the mean streamwise velocity  $\langle u \rangle(x_c, y)$  (left) and its associated fluctuating component  $\sqrt{\langle u'u' \rangle}(x_c, y)$  (right) for  $x_c/D = i/2$  with  $i = 1, \dots, 20$ . Comparison between our DNS (lines) and the experimental data of Maury et al. (2012) (symbols).

number in the simulation which leads to a higher level of dissipation by comparison to the experiment. Also, the increase of  $u'_{\text{rms}}$  on the centreline can be related to the turbulent diffusion of the turbulent fluctuations from the shear region toward the jet centre, a trend a priori more pronounced for relatively small Reynolds numbers.

As a conclusion for this section, a realistic turbulent jet is reproduced by simulation with a quantitative agreement with the experimental data in the near-nozzle region and a qualitative agreement further downstream. It suggests that even if the Reynolds number is relatively small by comparison to the experimental one, it is still possible to observe a fully turbulent flow for the natural jet. It is an important result as the main objective here is to control a jet in a turbulent regime. Another important point is the good quality of the inflow condition as proved by the good agreement between the experiment and the simulation in the near-nozzle region. The fact that the nozzle is included in the computational domain allows a direct comparison with experiments without any correction through the estimation of a virtual origin. To our knowledge, it is the first time that such a DNS/experiment comparison based on mean and fluctuating velocity data considered at strictly the same streamwise locations (i.e. without correction) is successfully obtained.

## 6. Comparison between the natural jet and the controlled jet

In this section, a comparison between the results obtained for a natural jet and a controlled jet is carried out based on turbulent statistics and instantaneous visualisations. Statistical data are obtained after a time average over a collection time of at least  $70D/U_c$ . To increase the statistical convergence, the statistics are also averaged in the azimuthal

direction for the natural jet. Note that it is the same level of convergence as in the previous section. For the controlled case, the symmetries of the configuration are used (azimuthal periodicity of  $\pi/4$  and mirror symmetry for each fluidevtron) leading to a major improvement of the statistics even if smaller than for the natural case. The instantaneous visualisations have been carefully chosen to illustrate the main physical features of the natural and controlled flows.

Note finally that the present study is explorative for the controlled jet with the fluidevtrons because the interaction between the actuators and the main jet is taken into account for the very first time. Only a selected part of the results is discussed in the following, with the main objective to check if the simulation can reproduce a realistic flow while showing consistent trends in reference to the experiments.

### 6.1. Mean velocity

The imprint from the microjets on the main jet can be directly observed on the mean streamwise velocity as shown in Figure 8. In this figure, 2D maps of the mean streamwise velocity are presented for different streamwise locations  $x/D = 0.1, 0.25, 0.5, 0.75, 1, 2, 4, 6$ . The distortion of the mean streamwise velocity induced by the microjets is clearly visible for the intermediate sections corresponding to  $x/D = 0.1, 0.25, 0.5, 0.75, 1, 2$ . A star pattern can be seen where the number of branches is related to the number of pairs of converging microjets. Further downstream, for  $x/D = 4, 6$  in Figure 8, a relaxation trend can be observed toward a more conventional azimuthally quasi-homogeneous round jet. The imprint of the microjets is no longer visible. Nevertheless, the strong velocity area where  $\langle u \rangle \approx U_c$  is more stretched by comparison to the natural jet, suggesting that the microjets tend to extend the potential core. This observation will be confirmed later.

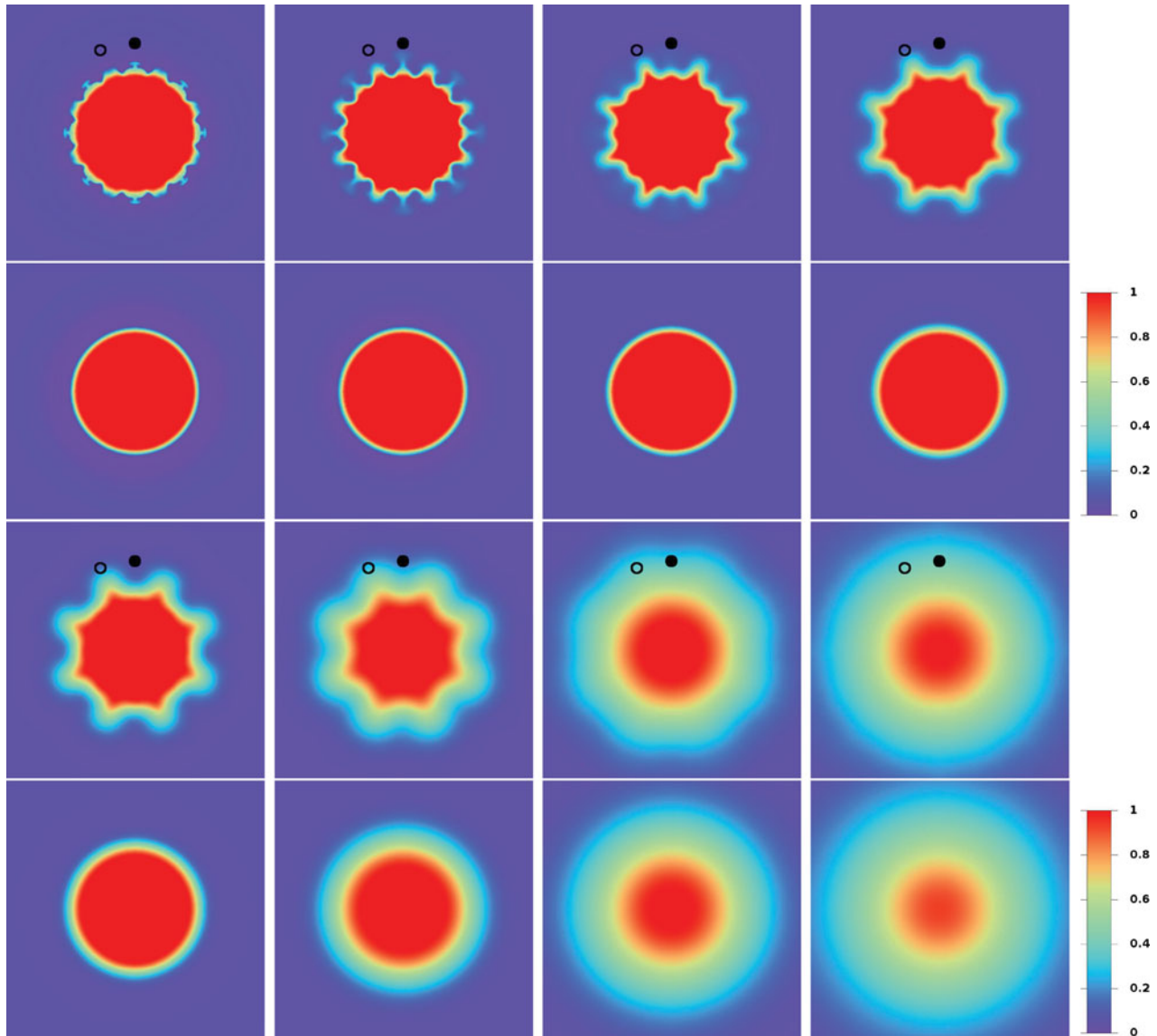


Figure 8. 2D maps of the mean streamwise velocity  $\langle u \rangle$  for  $x/D = 0.1, 0.25, 0.5, 0.75, 1, 2, 4, 6$ . The black dot is in the middle of a pair of converging microjets and the empty dot is between two pairs of converging microjets. Rows 1 and 3 correspond to the controlled jet and rows 2 and 4 to the natural jet.

To have a more complete view of the controlled flow, it could be interesting to analyse the layout of the radial velocity. 2D maps of the radial velocity are presented in Figure 9 for the same streamwise locations  $x/D = 0.1, 0.25, 0.5, 0.75, 1, 2, 4, 6$ . Only the controlled jet is presented as the radial velocity is virtually zero for the natural jet. A blue colour indicates a strong radial velocity toward the centre of the jet whereas a red colour indicates a strong radial velocity toward the surrounding of the jet. As expected in the near-nozzle region for  $x/D = 0.25, 0.5, 0.75, 1, 2$ , the blue areas correspond to the converging areas of the microjets, the latter producing an injection of fluid in the main jet. A notable observation is the ejection process that occurs

at shifted azimuthal locations to balance the injections of fluid from the converging microjets. This mechanism is responsible for the star shape observed previously on the mean streamwise velocity with branches located where the ejections happen. Further downstream, for  $x/D = 4, 6$  in Figure 9, the mean radial velocity is slowly reduced with a relaxation trend toward a more conventional round jet.

## 6.2. Turbulent kinetic energy

The previous observations based on the mean velocity field gave us an idea on how the main jet is affected by the microjets. However, the mean velocity field did not provide

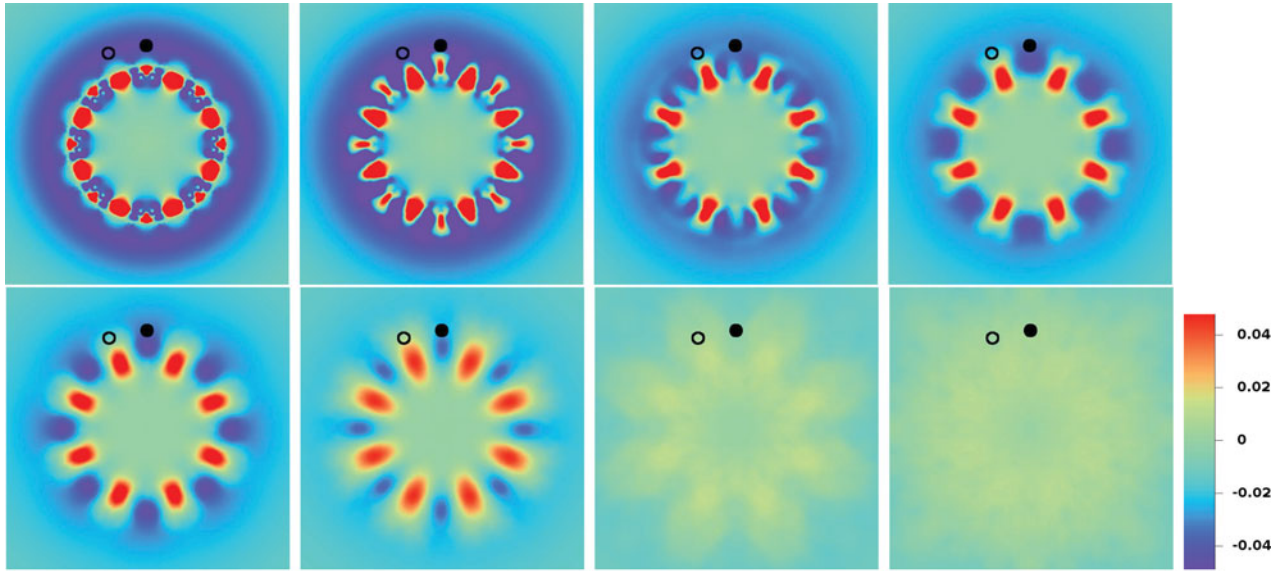


Figure 9. 2D map of the mean radial velocity  $\langle u_r \rangle$  for  $x/D = 0.1, 0.25, 0.5, 0.75, 1, 2, 4, 6$ . The black dot is in the middle of a pair of converging microjets and the empty dot is between two pairs of converging microjets (controlled jet only).

information about the production of unstable mechanisms resulting from the interaction between the microjets and the main jet. In order to quantify those mechanisms, 2D maps of the turbulent kinetic energy are presented in Figure 10. It can be seen that the microjets give rise to very high levels for the turbulent kinetic energy in the near-nozzle region for  $x < D$ . It is for  $x \approx 0.75D$  that those levels are at their highest. We can therefore assume that the interactions between the microjets and the main jet are very intense for this particular streamwise location through the production of highly energetic instabilities. In the next section, we will investigate the structures responsible for those instabilities. At this stage, we can observe that the turbulent kinetic energy  $k$  has maxima in the ejection areas observed previously on the mean radial velocity. Concerning the creation of instabilities, it seems that it is not the injections of fluid by the microjets which are efficient but more likely the associated ejections.

Further downstream for  $x > D$ , the situation is reversed with higher levels of turbulent kinetic energy for the natural jet. This inversion, in agreement with the experimental data (Laurendeau et al. 2008; Maury et al. 2012), can be directly observed in the  $x$ -planes presented in Figure 10. To locate more accurately the regions of turbulent fluctuations for the natural and controlled cases, the streamwise evolution of the spatially integrated turbulent kinetic energy

$$k_i(x) = \frac{1}{D^2} \int_{-\infty}^{+\infty} \int_{-\infty}^{+\infty} k \, dydz \quad (9)$$

is presented in Figure 11. Here, the spatial integration is done up to the computational domain boundary where  $k$  is

virtually zero. The comparison between the streamwise evolution of  $k_i(x)$  for each case allows the clear identification of the near-nozzle region  $0 < x < D$  where the microjets strongly contribute locally to the generation of turbulent fluctuations. Further downstream, the opposite influence can be observed with a significant reduction of  $k_i(x)$  by the microjets. For the controlled case, the strong generation of  $k$  in the near-nozzle region leads to a saturation of its maxima (see Figure 10) that is followed by a damping further downstream. Note that  $k_i(x)$  increases monotonically for both natural and controlled jets due to the increase of the volume where  $k \neq 0$  in the spatial integration of definition (9), even when the maxima of  $k$  are decreasing in the downstream region of the jets. The decrease of about 30% for  $k_i(x)$  at  $x \approx 5$  shown in Figure 11 for the controlled jet, by comparison to the natural jet, is consistent with the lengthening of its potential core.

### 6.3. Instantaneous visualisations

A global view of the vortex topology obtained for the natural and controlled jets is presented in Figure 12. The visualisations are based on the  $Q$ -criterion. Note that the two visualisations at the bottom of Figure 12 only show a slice for  $Q$  in the narrow central region  $|y| < 0.05D$ . This helps for the identification of large-scale structures as the associated motions are not hidden by the structures at the interface of the jet (top visualisations in Figure 12). This also enables the representation of the potential core plotted in yellow with an isosurface of the mean streamwise velocity such as  $\langle u \rangle = 0.95U_c$ .

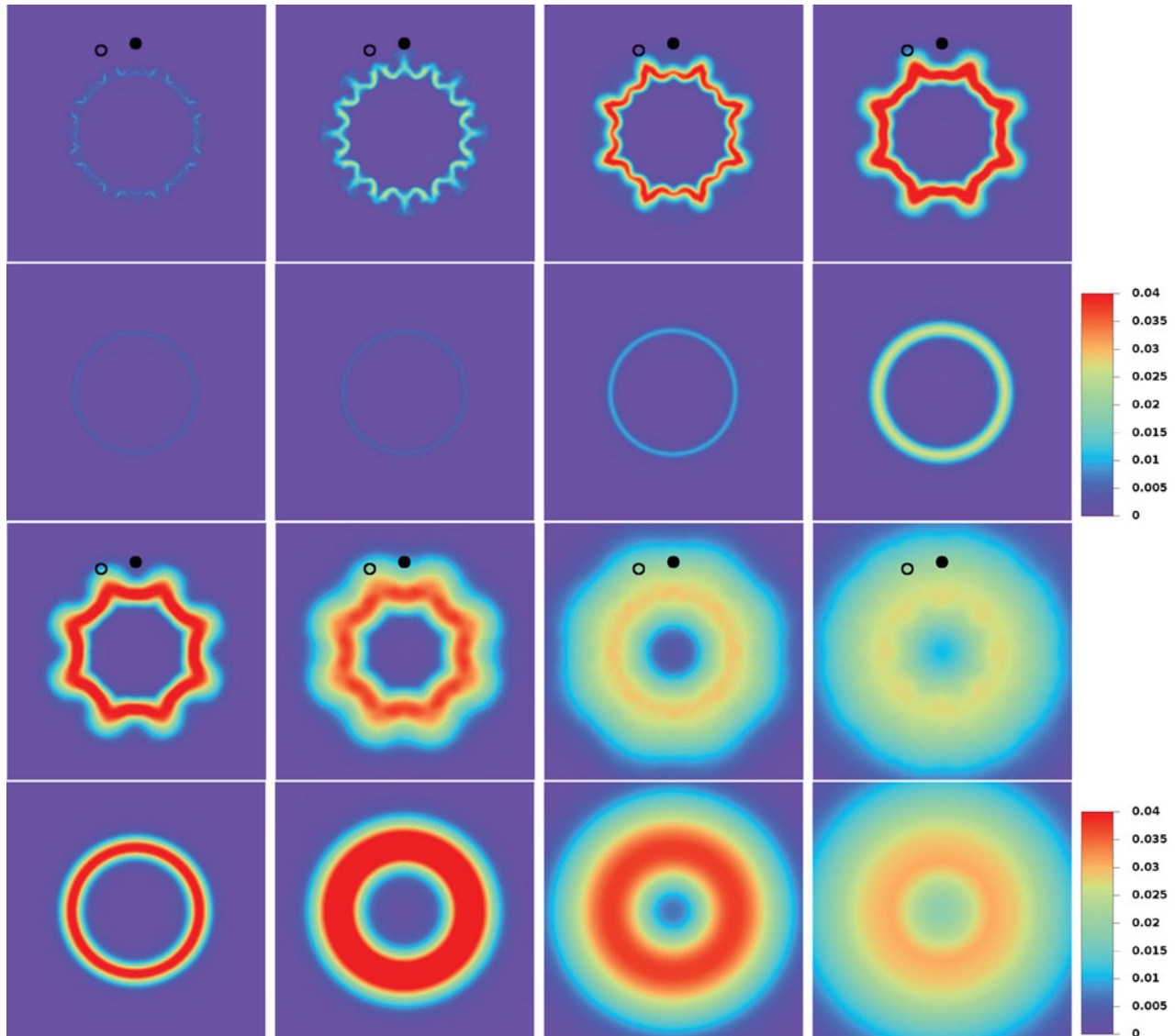


Figure 10. 2D map of the turbulent kinetic energy  $k = \frac{1}{2}(\langle u'u' \rangle + \langle v'v' \rangle + \langle w'w' \rangle)$  for  $x/D = 0.1, 0.25, 0.5, 0.75, 1, 2, 4, 6$  (normalised by  $U_c^2$ ). The black dot is in the middle of a pair of converging microjets and the empty dot is between two pairs of converging microjets. Rows 1 and 3 correspond to the controlled jet and rows 2 and 4 to the natural jet.

The comparison between the two visualisations at the top in Figure 12 leads to further observations. For the natural jet, we can clearly identify primary instabilities which are a distinctive feature of a round jet. As expected, those instabilities are Kelvin–Helmholtz like, with a strong azimuthal coherence. The frequency  $f$  associated with those ring-shape structures in the near-nozzle region can be estimated through the location of a distinct peak in the spectrum of the fluctuating radial velocity as shown in Figure 13. The main frequency  $f \approx 1.5U_c/D$  observed at  $x = 0.52D$  and  $x = D$  (see Figure 13 left and centre, respectively) provides a Strouhal number of  $St_\delta \approx 0.1$  based on the vorticity thickness of the main jet at the nozzle exit. This value is

in good agreement with literature values (see for instance Hussain and Zamam 1980). Further downstream, the primary structures are destabilised and a more turbulent state can be observed through a multiscale vortex dynamics as illustrated in the visualisations of Figure 12 but also more quantitatively as shown by the spectrum of the longitudinal velocity on the centreline at  $x = 8.5D$  (see Figure 13 right).

For the controlled case, none of those ring-shape structures can be observed in the visualisations. This absence of large-scale structures can also be confirmed with the energy spectra plots (see Figure 13 left and centre) in which no peak can be seen. It seems that there is no large-scale coherence for this flow. Straightaway after the lip of the

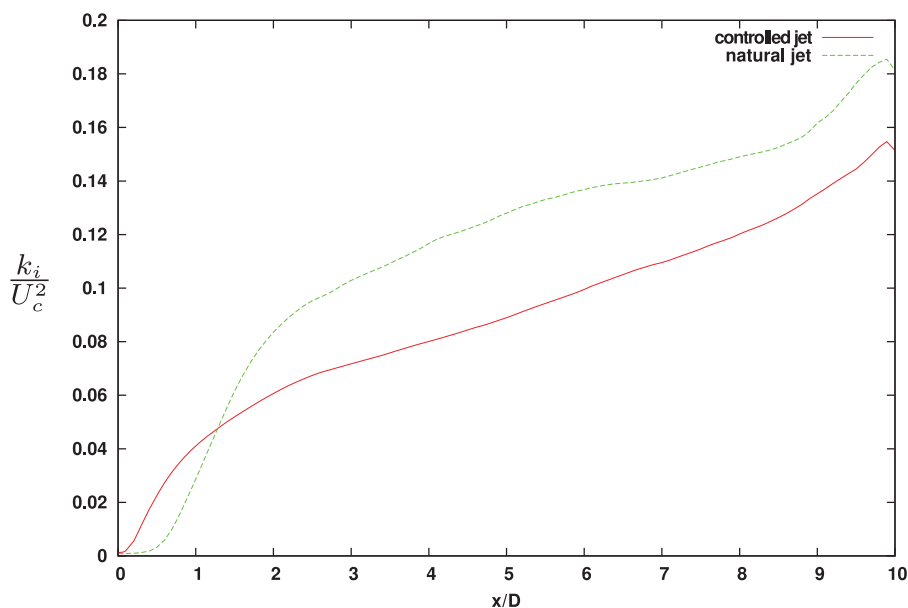


Figure 11. Streamwise evolution of the spatially integrated turbulent kinetic energy  $k_i(x)$  defined by Equation (9).

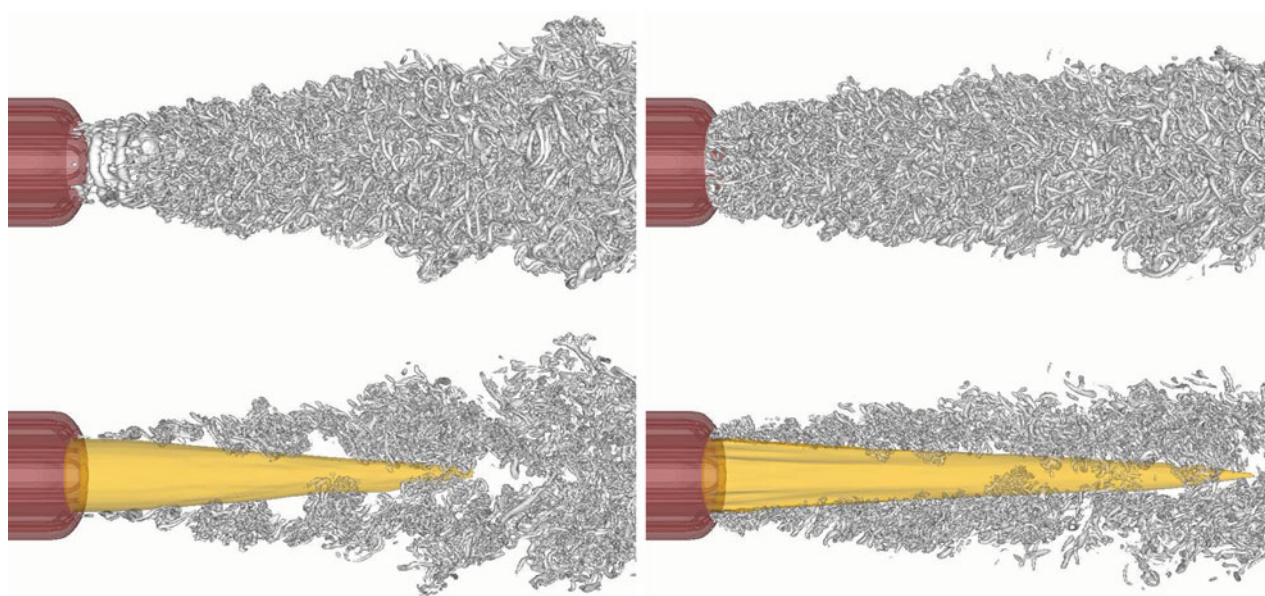


Figure 12. Isosurface for the  $Q$ -criterion for the 3D domain (top) and for only a slice  $|y| < 0.05D$  (bottom). The potential core boundary is shown in yellow with  $\langle u \rangle = 0.9U_c$ . Left corresponds to the natural jet and right to the controlled jet.

nozzle, very fine turbulent structures can be observed, resulting in a visual increase of the size of the main jet by comparison to the natural jet. The microjets seem to bypass the transition to turbulence by producing extremely quickly a fully turbulent state as suggested by the visualisations of Figure 12 or by the examination of the spectra in Figure 13 (left and centre) where a typical shape of turbulent spectrum is recovered very close to the nozzle lip contrary to the natural case. In reality, it is an artefact due to the reduced size of the transitional structures associated with the interaction

between the microjets and the main jet. More detailed visualisations of the near-nozzle region are presented in the next section.

Further downstream, the topology for the finest turbulent structures for the controlled jet is very similar to the one of the natural jet (see Figure 12, top) with the expected shape for a turbulent jet and an analogous spectral signature (see Figure 13 right). However, the visualisations at the bottom of Figure 12 indicate some differences for the large-scale structures of the jets. For the natural jet,

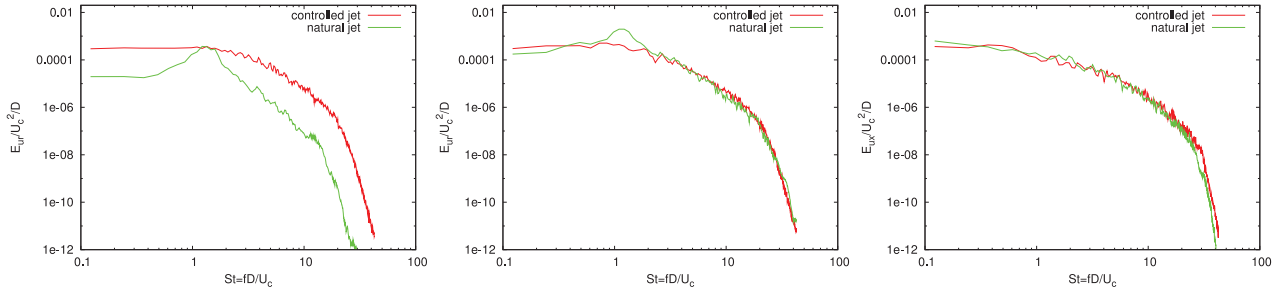


Figure 13. Fluctuating velocity spectra for the natural and controlled cases. Left: radial velocity  $u'_r$  in the vertical plane  $z = 0$  at  $r = D/2$  and  $x = 0.53D$ . Centre: radial velocity  $u'_r$  in the vertical plane  $z = 0$  at  $r = D/2$  and  $x = D$ . Right: longitudinal velocity  $u'_x$  on the centreline at  $x = 8.5D$ . Spectra are truncated at the cut-off frequency associated with the mesh  $f_{\Delta x} \approx 42.7U_c/D$ . The vertical plane  $z = 0$  is located in the middle of a pair of converging microjets.

turbulent puffs can be observed even far downstream from the nozzle. For the controlled jet, such large-scale intermittency cannot be seen. The mechanisms behind this fundamental modification are not easy to identify. As a first guess, we can argue that the microjets are accelerating the energy cascade toward the small scales straightaway in the near-nozzle region, the main persistent effect being the destruction of the large-scale coherence of the flow further downstream.

This acceleration of the energy cascade first produces higher levels of turbulent kinetic energy and then further downstream its saturation and damping as reported in Section 6.2. It seems reasonable to think that all these mechanisms contribute to the increase in length of the potential core which can clearly be seen in Figure 12. Qualitatively, this lengthening is quite substantial with an increase of +36% from  $5.5D$  to  $7.5D$ . Such a lengthening is in good agreement with the experimental observations of Laurendeau et al. (2008) and of Maury et al. (2012). Another mechanism that could potentially contribute to this lengthening is the ejection phenomenon. The ejections are connected to a strong production of turbulent kinetic energy as observed in section 6.2. The displacement of the regions with high production of  $k$  toward the ambient zone surrounding the jet reduces the influence of the instationarities on the centreline

jet dynamics. As a consequence, the potential core is more persistent despite the strong production of turbulent kinetic energy due to the microjets in the near-nozzle region.

#### 6.4. Identification of the near-nozzle structures

The overall view of the flow exhibited in Figure 12 is not helpful for the identification of the relatively small-scale primary instabilities for the controlled jet. In this section, our investigations focus on the region where the microjets are impacting the main jet. First, in order to confirm that the more active structures in the near-nozzle region for the controlled jet are smaller than the ones observed in the natural jet, we investigate the pressure field. The results are shown in Figure 14. By comparison to the  $Q$ -criterion, visualisations of the minima for the pressure field emphasise large-scale structures (Dubief and Delcayre 2000). This capability is used here as an advantage for the investigation of large-scale motions, investigations that cannot be done with the  $Q$ -criterion which is clearly more sensitive to small-scale structures for the vortex identification. In Figure 14, no large-scale structures can be clearly identified for the controlled jet (right) whereas for the natural jet (left), distinct large-scale ring-shape structures are observed in the near-nozzle region. The small-scale longitudinal structures

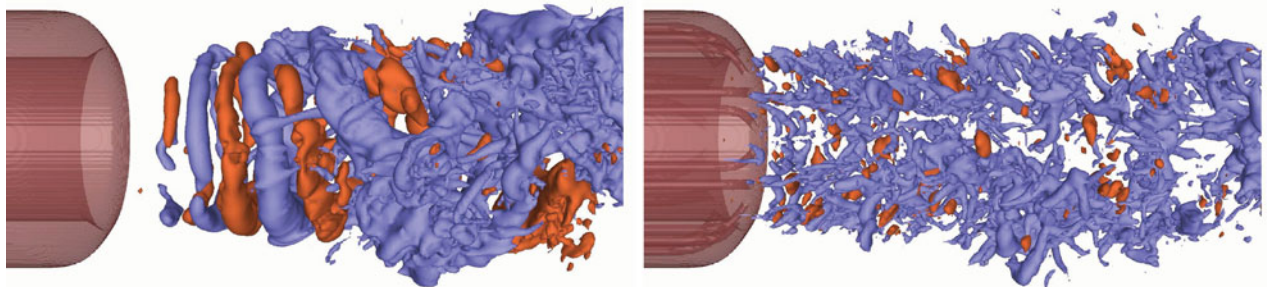


Figure 14. Pressure isosurfaces  $p = p_0 - 5.10^{-5}$  (blue) and  $p = p_0 + 5.10^{-5}$  (orange) for the natural jet (left) and the controlled jet (right).

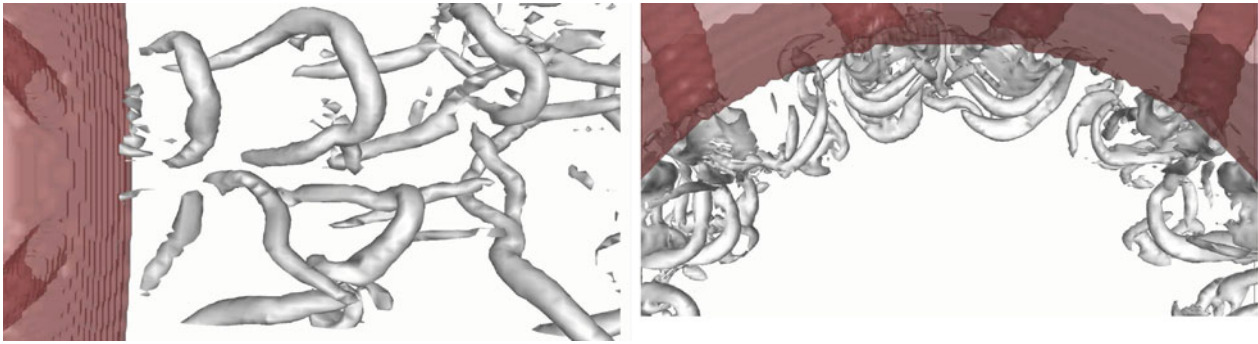


Figure 15. Isosurface for the  $Q$ -criterion where the more intense horseshoe structures (with the number **1** in Figure 16) can be seen. The left visualisation is enlarged near a pair of converging microjets and the right one is a view from the inside of the main jet.

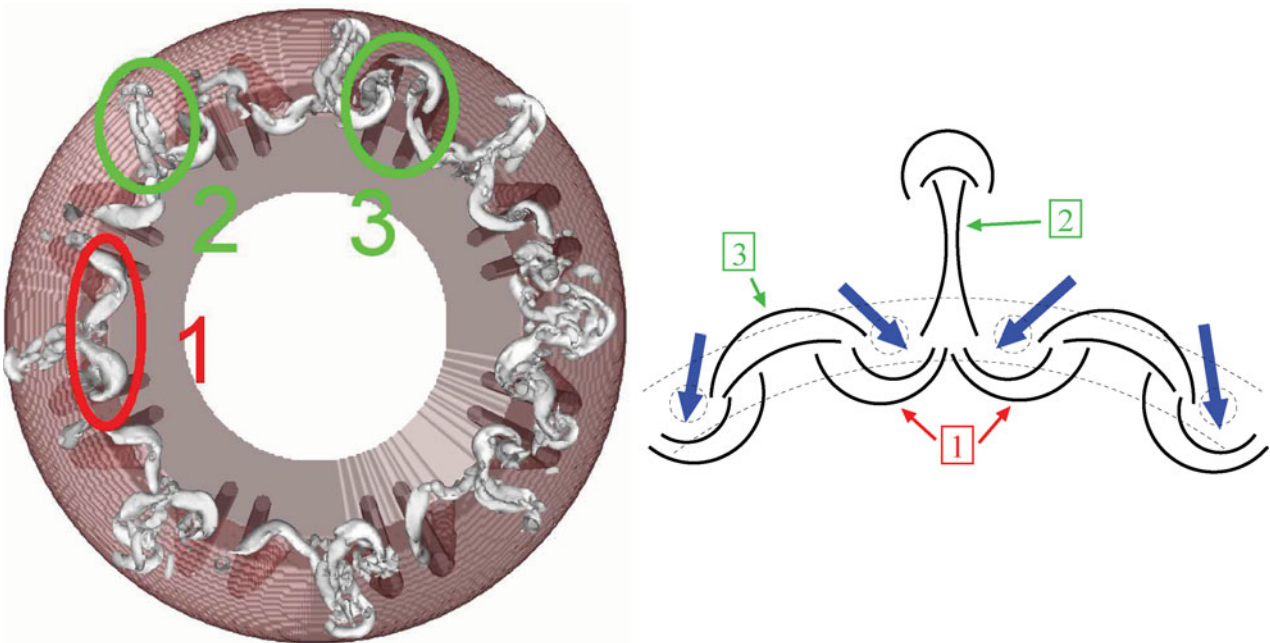


Figure 16. Identification of the three coherent structures in the near-nozzle region for  $0 < x/D < 0.5$  with a  $Q$ -criterion visualisation (left) and a schematic sketch behind four microjets (right).

produced as a result of the interaction between the microjets and the main jet cannot be identified with the pressure field. However, it is clear that for the controlled jet, the flow loses its azimuthal coherence not only in the near-nozzle region but even further downstream where the finest scales for the controlled jet are much smaller than the finest scales from the natural jet.

In order to have a more accurate idea of the small-scale structures generated by the interaction between the microjets and the main jet, zoom views of the  $Q$ -criteria are presented in Figure 15 for the controlled jet. Horseshoe patterns can clearly be seen at the exit of the nozzle in the region where two convergent microjets are injecting fluid into the main jet. Based on these visualisations, it is possible to distinguish clearly the periodic formation of pairs of

horseshoe structures near the microchannels. Those structures, created as a result of the microjets impacting with the shear layer of the main jet, are interacting with each other further downstream. We can interpret the occurrence of those structures as the main mechanism responsible for the high levels of turbulent kinetic energy observed previously. Because of their shape and orientation, they mainly influence the internal region of the shear layer of the main jet. In the schematic view in Figure 16, the horseshoe structures are indicated with the number **1**. An important point is that those structures could not be reproduced if the microchannels were not taken into account in the computational domain. If a forcing term was used to model the microjets then none of the horseshoe structures would have been reproduced realistically. Horseshoe structures are

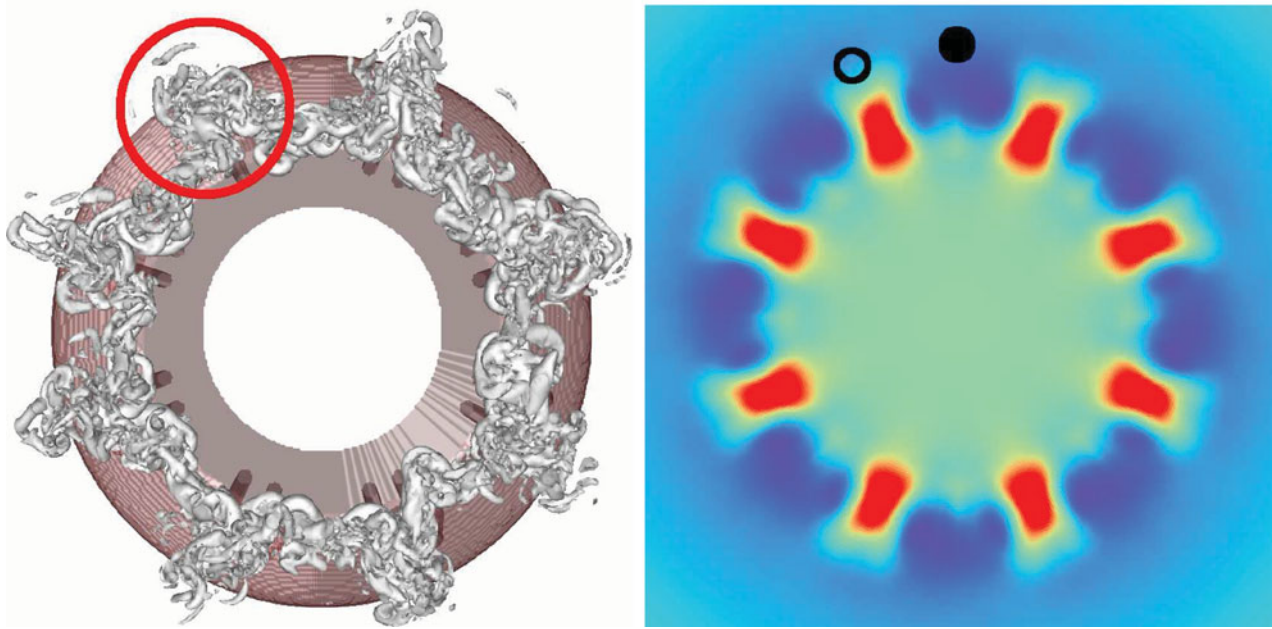


Figure 17. Visual link between the ejected structures at the interface of the main jet for  $0.5 < x/D < 0.7$  using the  $Q$ -criterion (left) and the mean radial velocity  $\langle u_r \rangle$  for  $x/D = 0.6$  (right).

generated by a pulsed mechanism involving a flapping of the microjets when they interact with the main jet, a feature that cannot be reproduced with a simple forcing term. The realistic modelling of this interaction is the main justification for the consideration of the present highly complex nozzle geometry with the help of an improved IBM.

Further downstream for  $0.25D < x < 0.5D$ , the development of turbulent structures in the outer region of the main jet can be observed. Those structures, indicated by the number [3] in Figure 16, are generated between two pairs of converging microjets. Similar structures can be observed at the same radial position but this time within pairs of converging microjets. The latter structures are indicated with the number [2]. They seem to lead to stronger ejections of fluid but are significant only in the near-nozzle region. On the contrary, even if structures [3] are quite weak for  $0.25D < x < 0.5D$ , they become very intense for  $0.5D < 0 < 1.5D$  with a significant contribution to the development of the turbulence in the outer region of the main jet. This can be clearly observed in Figure 17 where the link between highly intense structures (from the ejections) with an important radial velocity from the middle of the jet toward its surrounding is highlighted. The star shape observed initially on the mean streamwise velocity profile is recovered here with an instantaneous visualisation of the turbulent structures. An important remark is that the ejections coexist with the development of small-scale turbulent structures, giving rise to an early development for the turbulence in the controlled jet. This early development takes place mainly at the outer region of the jet, explaining why the length of

the potential core is enhanced and not reduced despite the accelerated production of turbulent kinetic energy.

## 7. Discussion and conclusions

One of the main purposes of this numerical work is to demonstrate the feasibility for a DNS to accurately reproduce a microjet device used to control a turbulent jet by taking into account its geometry inside the computational domain. To achieve this, an improved IBM has been developed. This new IBM is compatible with the use of supercomputers and with the requirement of high-order schemes in terms of accuracy and reduction of spurious numerical oscillations. After a careful validation with the flow around a cylinder, two simulations have been performed of a turbulent jet with and without fluidic control.

For the numerical side, the use of an IBM does not guarantee the mass conservation of the system from a discrete point of view and it is very important to pay attention to this problem for any simulation. For instance, with the marginal resolution inside the microchannels due to numerical constraints, a small error on the verification of the divergence-free condition can lead to a quite substantial loss of mass within the system. To deal with this problem, the retraction of  $\varepsilon$  was essential with a distinct amelioration of the realism of the solution. However, this point is still under careful examination and new developments are currently under revision for a better mass conservation, following the recent development of Bouchon, Dubois, and James (2012) and Cheny and Botella (2010).

For the physical side, the simulation with the controlled jet clearly exhibits the importance of a realistic modelling of the interaction between the microjets and the main jet. This point alone justifies the present numerical approach where the modelling of the microjets is performed explicitly. In their interactions with the main jet, the microjets are subjected to a flapping mechanism which gives rise to horseshoe structures in the near-nozzle region. This phenomenon can be identified as the primary mechanism for the injection of small-scale structures inside the main jet.

To balance this injection of fluid by the microjets in the core of the main jet, an ejection mechanism is observed further downstream. This secondary mechanism, responsible for the increase of the levels of turbulent kinetic energy, is strongly correlated with the primary mechanism previously described. Not only this secondary mechanism increases the kinetic energy, it also moves it toward the outer region of the jet. The dramatic increase of the turbulent kinetic energy by the microjets leads to a saturation and then a damping of the turbulence with lower levels of energy further downstream of the jet by comparison to the natural jet. This effect, combined with the displacement of the energy toward the outer region of the main jet, is responsible for the lengthening of the potential core, in good agreement with the experimental observations. For the first time, this simulation provides a physical explanation for this rather paradoxical mechanism where the potential core is more persistent despite the early injection of turbulent fluctuations. The importance of these ejections between pairs of microjets is a first hint about the specific role of the convergence property of the microjets for the present device.

Another notable point, even if it is more qualitative, is the lack of large-scale structures for the controlled jet by comparison to the natural jet. This difference was expected in the near-nozzle region of the jet as the 16 microjets inevitably perturb azimuthally the main jet. Surprisingly, this is also true further downstream where the flow is fully established. The persistence of large-scale structures is clearly visible for the natural jet but is not for the controlled jet. In terms of spatial scales, it seems that the small-scale injection of fluctuating energy via the microjets prevents somehow the occurrence of large-scale coherent structures with persistent effects further downstream, in the fully developed turbulent region of the main jet.

To summarise, microjets speed up the development of the turbulence with a strong generation of fluctuations just after the lip of the nozzle. This injection of fluctuating energy happens at small scales or equivalently at high frequencies. In an aeroacoustic framework where these fluctuations are interpreted as acoustic sources, it is reasonable to think that their amplification will generate sound at higher frequencies by comparison to the natural jet. Such a mechanism would be consistent with the experiments of Laurendeau et al. (2008) and of Maury et al. (2012) where the authors observed an increase of the noise for high

frequencies for the controlled jet. In a same way, the lack of large-scale structures, such as the ring-shape structures in the near-nozzle region, could more likely be responsible for the reduction of noise emission at low frequencies. In terms of practical applications, this noise reduction at low frequencies is an advantage because it concerns frequencies that a human person is more likely going to be affected by. This reduction was clearly observed in the experiments and the present simulations suggest a simple mechanism through a change of the spectral component of the acoustic sources in the main jet.

At this stage, the relationship between the flow dynamic and the sound emission is purely speculative. An interesting development would be to carry out an acoustic analogy by using the present incompressible data following a strategy used by Laizet et al. (2012). The reproduction of the decrease/increase of noise at low/high frequencies would certainly help in our understanding for such a flow and would offer more relevant data to define the best configuration to reduce the noise of a turbulent jet with a fluidevtron device.

### Acknowledgements

This work was granted access to the HPC resources of IDRIS/CINES/CCRT under the allocation 2012/2013-020912 made by GENCI (Grand Equipement National de Calcul Intensif). The authors are grateful to Rémy Maury, Peter Jordan and André Cavalieri for providing the experimental data and for helpful discussions about the physical analysis for the present flow configuration.

### Notes

1. This open source code is now available at <http://code.google.com/p/incompact3d/>.
2. In order to impose as precisely as possible the flow rate inside the microchannels, a Poiseuille-like extra forcing was imposed in their straight part for  $x < -0.5D$ .

### References

- Arakeri, V. H., A. Krothapalli, V. Siddavaram, M. B. Alkisar, and L. M. Lourenco. 2003. "On the Use of Microjets to Suppress Turbulence in a Mach 0.9 Axisymmetric Jet." *Journal of Fluid Mechanics* 490: 75–98.
- Bouchon, F., T. Dubois, and N. James. 2012. "A Second-Order Cut-Cell Method for the Numerical Simulation of 2D Flows Past Obstacles." *Computers & Fluids* 65: 80–91.
- Castelain, T., M. Sunyach, D. Juvé, and J.-C. Bera. 2008. "Jet-Noise Reduction by Impinging Microjets: An Acoustic Investigation Testing Microjet Parameters." *AIAA Journal* 46 (5): 1081–1087.
- Cheny, Y., and O. Botella. 2010. "The LS-STAG Method: A New Immersed Boundary/Level-Set Method for the Computation of Incompressible Viscous Flows in Complex Moving Geometries with Good Conservation Properties." *Journal of Computational Physics* 229 (4): 1043–1076.
- Chorin, A. 1968. "Numerical Simulation of the Navier-Stokes Equations." *Mathematics of Computation* 22: 745–762.

- Dubief, Y., and F. Delcayre. 2000. "On Coherent-Vortex Identification in Turbulence." *Journal of Turbulence* 1: 011.
- Fadlun, E. A., R. Verzico, P. Orlandi, and J. Mohd-Yusof. 2000. "Combined Immersed-Boundary Finite-Difference Methods for Three-Dimensional Complex Flow Simulations." *Journal of Computational Physics* 161: 35–60.
- Gautier, R., D. Biau, and E. Lamballais. 2013. "A Reference Solution of the Flow over a Circular Cylinder at  $Re = 40$ ." *Computers & Fluids* 75: 103–111.
- Goldstein, D., R. Handler, and L. Sirovich. 1993. "Modeling a No-Slip Boundary Condition with an External Force Field." *Journal of Computational Physics* 105: 354–366.
- Hasan, N., S. F. Anwer, and S. Sanghi. 2005. "On the Outflow Boundary Condition for External Incompressible Flows: A New Approach." *Journal of Computational Physics* 206: 661–683.
- Hussain, A., and K. Zamam. 1980. "Vortex Pairing in a Circular Jet Under Controlled Excitation. Part 2. Coherent Structure Dynamics." *Journal of Fluid Mechanics* 101: 493–544.
- Kravchenko, A. G., and P. Moin. 1997. "On the Effect of Numerical Errors in Large Eddy Simulation of Turbulent Flows." *Journal of Computational Physics* 131: 310–322.
- Laizet, S., V. Fortuné, E. Lamballais, and J. C. Vassilicos. 2012. "Low Mach Number Prediction of the Acoustic Signature of Fractal-Generated Turbulence." *International Journal of Heat and Fluid Flow* 35: 25–32.
- Laizet, S., and E. Lamballais. 2009. "High-Order Compact Schemes for Incompressible Flows: A Simple and Efficient Method with Quasi-spectral Accuracy." *Journal of Computational Physics* 228: 5989–6015.
- Laizet, S., and N. Li. 2011. "Incompact3d: A Powerful Tool to Tackle Turbulence Problems with up to  $O(10^5)$  Computational Cores." *International Journal for Numerical Methods in Fluids* 67 (11): 1735–1757.
- Lamballais, E. 2014. "Direct Numerical Simulation of a Turbulent Flow in a Rotating Channel with a Sudden Expansion." *Journal of Fluid Mechanics* 745: 92–131.
- Lamballais, E., V. Fortuné, and S. Laizet. 2011. "Straightforward High-Order Numerical Dissipation via the Viscous Term for Direct and Large Eddy Simulation." *Journal of Computational Physics* 230: 3270–3275.
- Lamballais, E., and J. Silvestrini. 2002. "Direct Numerical Simulation of Interactions Between a Mixing Layer and a Wake Around a Cylinder." *Journal of Turbulence* 3: 028.
- Lamballais, E., J. Silvestrini, and S. Laizet. 2008. "Direct Numerical Simulation of a Separation Bubble on a Rounded Finite-Width Leading Edge." *International Journal of Heat and Fluid Flow* 29 (3): 612–625.
- Lamballais, E., J. Silvestrini, and S. Laizet. 2010. "Direct Numerical Simulation of Flow Separation Behind a Rounded Leading Edge: Study of Curvature Effects." *International Journal of Heat and Fluid Flow* 31 (3): 295–306.
- Laardeau, S., E. Lamballais, and J.P. Bonnet. 2002. "Direct Numerical Simulation of a Jet Controlled by Fluid Injection." *Journal of Turbulence* 3: 002.
- Laurendeau, E., P. Jordan, J.-P. Bonnet, J. Delville, P. Parnaudeau, and E. Lamballais. 2008. "Subsonic Jet Noise Reduction by Fluidic Control: The Interaction Region and the Global Effect." *Physics of Fluids* 20: 101519.
- Lele, S. K. 1992. "Compact Finite Difference Schemes with Spectral-Like Resolution." *Journal of Computational Physics* 103: 16–42.
- Li, N., and S. Laizet. 2010. "2DECOMPFFT – A Highly Scalable 2D Decomposition Library and FFT Interface." Cray User Group 2010 Conference, Edinburgh, TX, May 24–27.
- Maury, R., M. Koenig, L. Cattafesta, P. Jordan, and J. Delville. 2012. "Extremum-Seeking Control of Jet Noise." *Int. J. Aeroacoustics* 11 (3–4): 459–474.
- Maury, R., M. Koenig, L. Cattafesta, P. Jordan, J. Delville, J. P. Bonnet, and Y. Gervais. 2009. "Extremum-Seeking Optimisation of Fluidic Jet-Noise Control." Proceedings of the 15th AIAA/CEAS Aeroacoustics Conference, Miami, FL, May 11–13.
- Parnaudeau, P., J. Carlier, D. Heitz, and E. Lamballais. 2008. "Experimental and Numerical Studies of the Flow over a Circular Cylinder at Reynolds Number 3 900." *Physics of Fluids* 20: 085101.
- Parnaudeau, P., E. Lamballais, D. Heitz, and J. Silvestrini. 2004. "Combination of the Immersed Boundary Method with Compact Schemes for DNS of Flows in Complex Geometry." In *Direct and Large-Eddy Simulation V, ERCOFTAC Series*, edited by R. Friedrich, B. J. Geurts, and O. Métais, 581–590. Kluwer Academic, held at the Munich University of Technology, August 27–29, 2003.
- Raman, G. 1997. "Using Controlled Unsteady Fluid Mass Addition to Enhance Jet Mixing." *AIAA Journal* 35 (4): 647–656.
- Shur, M. L., P. R. Spalart, and M. Kh. Strelets. 2010. "LES-Based Evaluation of a Microjet Noise Reduction Concept in Static and Flight Conditions." *Procedia Engineering* 6: 44–53.
- Silvestrini, J. H., and E. Lamballais. 2002. "Direct Numerical Simulation of Wakes with Virtual Cylinders." *International Journal of Computational Fluid Dynamics* 16 (4): 305–314.
- Silvestrini, J., and E. Lamballais. 2004. "Direct Numerical Simulation of Oblique Vortex Shedding from a Cylinder in Shear Flow." *International Journal of Heat and Fluid Flow*, 25 (3): 461–470.
- Temam, R. 1969. "Sur l'approximation de la solution des équations de Navier-Stokes par la méthode des pas fractionnaires II." *Archive for Rational Mechanics and Analysis* 32: 377–385.